Mathematical Medicine and Biology (2014) **31**, 99–124
doi:10.1093/imammb/dqs031
Advance Access publication on January 28, 2013

The role of contractile unit reorganization in force generation in airway smooth muscle

B. S. Brook*
School of Mathematical Sciences, University Park, University of Nottingham, Nottingham NG7 2RD, UK
*Corresponding author: bindi.brook@nottingham.ac.uk

AND

O. E. Jensen
School of Mathematics, University of Manchester, Oxford Road, Manchester M13 9PL, UK

[Received on 17 May 2012; revised on 4 October 2012; accepted on 4 November 2012]

Airway smooth muscle (ASM) cells undergo remodelling and reside in a tissue structure that is subject to heterogenous stress distributions that change dynamically during the breathing cycle. In this paper, we develop a structural model of an ASM cell that consists of contractile units (actin and myosin filaments) in series and parallel, anchored to a nonlinearly elastic cytoskeleton. We mimic a typical experimental protocol that involves isometric force generation through triggering of the contractile machinery, followed by oscillatory length fluctuation of the cell. We use the model to predict the effect of a single instance of rearrangement of the contractile machinery, combined with strain-stiffening of the cytoskeleton, on the force generated by the sarcomeres, and the total force generated by the cell. By linking intra-cellular events to whole-cell behaviour, the model reveals mechanistic relationships between structural properties and cell-level force–length loops. We show how contractile force, shortening velocity and sarcomere operating lengths vary as the internal cell architecture is altered. Additionally, we show how interactions between the internal contractile machinery and cytoskeletal structure play a role in the regulation of force generation and hysteresis of the cell.

Keywords: airway smooth muscle, contractile unit, plasticity, serial-to-parallel transitions.

1. Introduction

In chronic asthma, airway remodelling as a result of increased airway smooth muscle (ASM) is a well-known phenomenon (Brightling *et al.*, 2012). The elastic stress distributions in a remodelled (and therefore thickened, relative to the lumen) airway wall are predicted to be highly heterogenous, with different regions experiencing either tensile or compressive hoop and radial stresses (Brook *et al.*, 2010). This suggests that ASM cells within the wall are likely to be in different stress micro-environments depending on their position in the airway wall. The ability of ASM to adapt to changes in length and maintain maximal force generation over a large length range (Gunst *et al.*, 1995; Pratusevich *et al.*, 1995) appears to require plastic changes in sub-cellular structures that involve rearrangement of contractile units within the contractile apparatus and reshaping of the apparatus itself. Smooth muscle cell plasticity has also been demonstrated via force-fluctuation-induced re-lengthening of ASM cells (Dowell *et al.*, 2005, 2010). In order to understand the effect of different stress environments (particularly the dynamic changes during tidal breathing) on the contractility and plasticity of the ASM and

hence on the airway, a bottom-up approach seems necessary to account for the multitude of mechanisms operating at the cell- and sub-cellular levels.

A number of mathematical models have been proposed that address different aspects of smooth muscle plasticity, such as the stochastic percolation model of Silveira *et al.* (2005) and the overlap one-dimensional (1D) model developed by Lambert (2004). However, these models do not incorporate the molecular mechanisms of force generation. Fredberg *et al.* (1999) and Mijailovich *et al.* (2000) based their models of active force generation on the cross-bridge mechanisms that occur in the smooth muscle cell, combining the original sliding-filament model of Huxley (1957) (which accounts for actin-myosin interactions) and the Hai–Murphy four-state model (Hai & Murphy, 1988a,b). These have subsequently been further developed and used by Wang *et al.* (2008), Politi *et al.* (2010) and Lauzon *et al.* (2012) in larger multi-scale models coupling molecular interactions to organ-level mechanics. In addition, there is a growing consensus that while acto-myosin cross-bridge dynamics are key (Fredberg *et al.*, 1999; Mijailovich *et al.*, 2000), they are not sufficient to explain all the observed behaviour of the ASM cell. Emerging data support the view of the actin cytoskeleton of smooth muscle cells as a dynamic structure (evolving through actin (de-)polymerization) which, in concert with active force-generation mechanisms, could play an integral role in regulating the development of mechanical tension and the material properties of smooth muscle tissues (Gunst & Fredberg, 2003; Gunst & Zhang, 2008; Mehta & Gunst, 1999; Zhang & Gunst, 2008). None of the models described above, however, account for force-generation, cytoskeletal dynamics and plasticity in a comprehensive quantitative model of the ASM cell as a self-contained structure that forms part of a composite tissue.

In order to link the multitude of intra-cellular events to behaviour at the level of the whole cell and thus eventually to ASM tissue, we develop here a new model of an individual ASM cell that incorporates molecular cross-bridge interactions and cytoskeletal properties and the effects of contractile unit re-arrangement. We assess the ability of such a model to explain biomechanical observations from experimental protocols that are commonly used to investigate contractile and mechanical properties of ASM tissue. Typically a strip of tissue is taken from an airway and the length of the strip is held fixed, while a known amount of agonist is added. The agonist triggers contraction which evolves until a maximal isometric force is generated. The strip is then stretched sinusoidally. Contractile force is measured and plotted against the length of the strip. Typical force–length loops (taken from Bates *et al.*, 2009) are shown in Fig. 1. In their paper, Bates *et al*. used a one-dimensional model for the tissue in which a nonlinear viscoelastic Kelvin–Voigt element is in series with a single active force generator, all in parallel with a second nonlinear Kelvin–Voigt body, to account for the passive and active properties of the strip. They were able to show that by selecting appropriate nonlinearity for the elastic and viscoelastic elements, the observed ‘banana-shape’ force–length loops could be reproduced to some extent. While this phenomenological tissue-scale model is useful, we believe that modelling individual cells, and their intra-cellular structure, will more clearly reveal the mechanistic basis for the nonlinear expressions used by Bates *et al*.

We begin this task by considering a simplified model of an individual ASM cell, accounting for nuclear, contractile unit and cytoskeletal mechanical properties. The complexity of the numerous interactions necessitates simplification of some of the mechanisms in order to understand thoroughly the effect of different intra-cellular structural elements on overall cell behaviour. At this initial stage our model allows us to explore the effect of changes in the cell’s internal architecture arising from externally imposed strain and reveals the contributions of different elements to cell-level force–length loops.

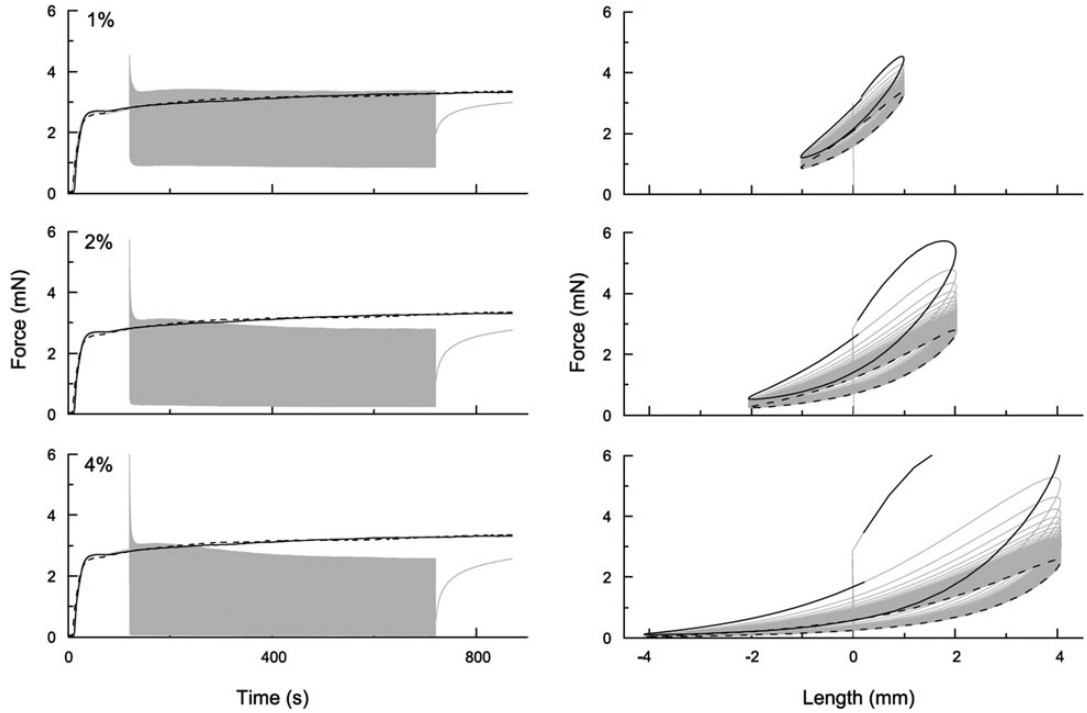

FIG. 1. Force–time and force–length traces obtained in a strip of rat trachealis muscle. The grey curves show data obtained with 2 Hz length oscillations having amplitudes of ±1, ±2, and ±4% L_{ref} as indicated, where L_{ref} is the unstressed, resting length of the tissue strip. Isometric force–time curves are shown in black (at left; solid lines obtained before collecting oscillation data, dashed lines obtained afterwards). The black curves (at right) show the first (solid line) and last (dashed line) force–length loops obtained during length oscillation. Reproduced with permission from Bates *et al.* (2009).

2. Methods

2.1 *1D cell model*

On the basis of the conceptual model of ASM cell structure proposed by Kuo & Seow (2004) (see Fig. 2), we propose a 1D model of a smooth muscle cell as depicted in Fig. 3. We assume that contractile units consisting of a myosin and two actin filaments connect to other contractile units via dense bodies in series as depicted in Fig. 4. (We will refer to these contractile units as sarcomeres although they are different in structure from the sarcomeres found in striated muscle.) The sarcomeres anchor via focal adhesions to the cell cytoskeleton directly or in series with the cell nucleus and cytoskeleton (Kuo & Seow, 2004). We thus assume for simplicity that the sarcomeres form two types of rows (termed A and B in our model) as depicted in Fig. 3. Histological sections of muscle cells (Kuo & Seow, 2004) provide information about the proportion of sarcomeres present in the cell that connect to the nucleus via actin filaments and dense bodies (type A), and the proportion that connect directly to the cytoskeleton (type B). In the present study, we model a single instance of the rearrangement of these contractile units because of an imposed length change of the whole cell.

In the model presented below, starred quantities are dimensional and bars denote quantities at maximally activated steady-state isometric conditions. At any time t^* the length of an individual cell $L^*(t)$

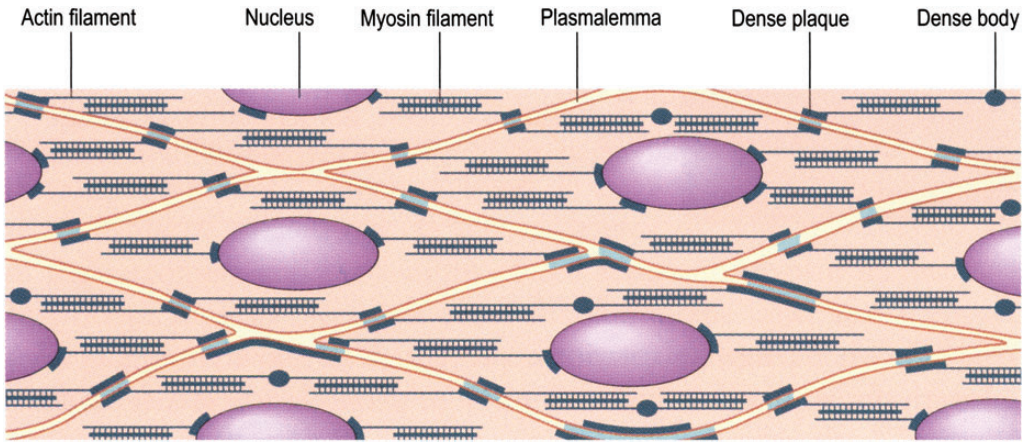

FIG. 2. Schematic of contractile filament architecture in a bundle of ASM cells. Reproduced with permission from Kuo & Seow (2004).

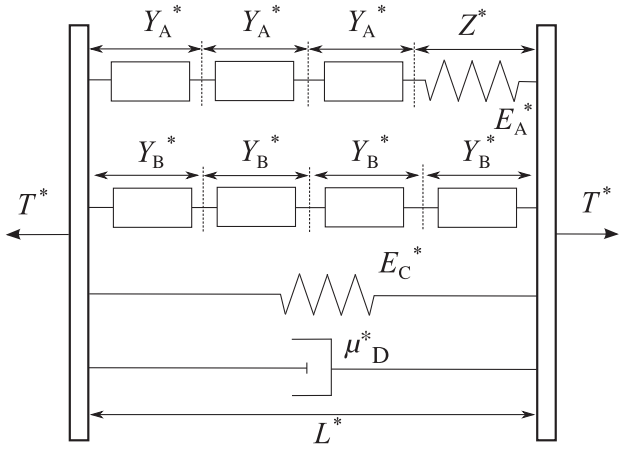

FIG. 3. Model of a single ASM cell, consisting of contractile units or sarcomeres of length Y_A^*, each generating a force F_A^* connected to a relatively stiff nucleus (stiffness E_A^*) in parallel with contractile units of length Y_B^*, connected only to the cytoskeleton, each generating a force F_B^*. The elasticity of the cytoskeleton itself is depicted as another spring in parallel with stiffness E_C^*. The effect of the extensional viscosity of the whole cell, is represented as a dashpot in parallel, with extensional viscosity μ_D^*.

and the lengths of the individual sarcomeres $Y_A^*(t^*)$ and $Y_B^*(t^*)$ (see Fig. 3) satisfy

$$L^* = N_A^* Y_A^* + Z^* = N_B^* Y_B^*, \tag{2.1a}$$

where N_A^* and N_B^* are the number of sarcomeres connected in rows A and B, respectively. We assume that all the sarcomeres in each row are identical. The total number of sarcomeres is $N_S^* = N_A^* + N_B^*$. We assume that either N_A^* and N_B^* are constants for all time, or piecewise constant, with instantaneous change in their value from their initial state $\overline{N}_A^*, \overline{N}_B^*$, to some new value, while ensuring that N_S^* is

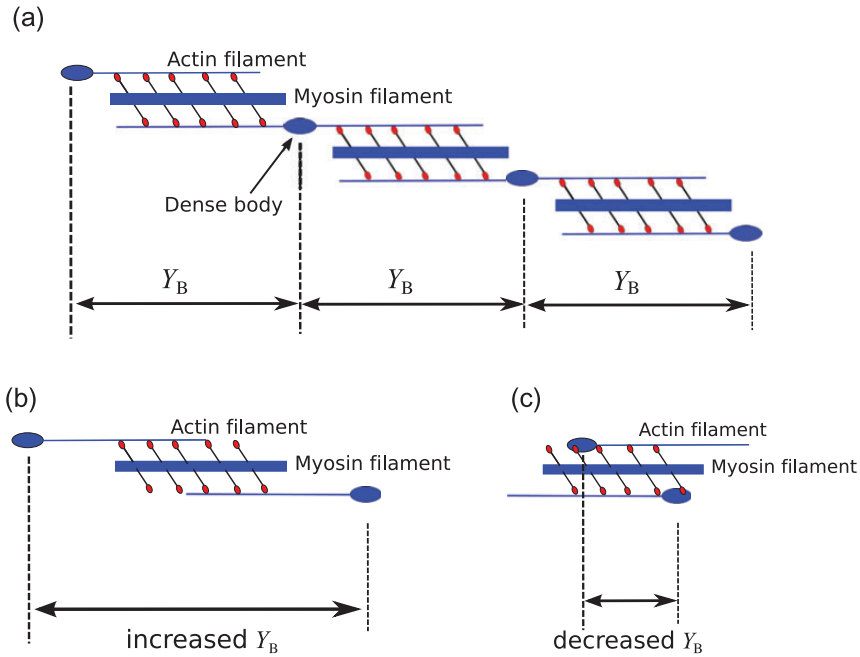

FIG. 4. (a) Schematic of a row of ASM contractile units in series. The row depicted here is row B, the contractile units connect to the cytoskeleton via membrane adhesion complexes. (b) Reduction in the number of available cross-bridges as a result of stretch and the reduction in the overlap length between actin and myosin filaments. (c) Reduction in the overlap length via compression and hence a reduction in the number of available cross-bridges.

conserved, to mimic contractile apparatus rearrangement at a particular time. Typical parameter values for these quantities and others that follow below are given in Table 1.

The total force, T^*, that the cell exerts (which may be tensile or compressive) on its neighbours is given by the sum of the forces in each of the parallel contributions. Balancing forces, it follows that

$$T^* = F_A^* + F_B^* + E_C^*(L^* - L_0^*) + \mu_D^* \dot{L}^*, \tag{2.1b}$$

where

$$F_A^* = E_A^*(Z^* - Z_0^*), \tag{2.1c}$$

the dot over L in (2.1b) denotes a time derivative. L_0^* and Z_0^* are the unstressed cell and nucleus length, respectively. The stiffness of the cytoskeleton, E_C^*, represented by the spring in Fig. 3, can vary by several orders of magnitude and is thought to depend on the strain amplitude and rate (Chen *et al.*, 2010; Krishnan *et al.*, 2009). We, however, note that these reported measures are related to the cell stiffness measured immediately after the cell has been transiently stretched and then returned to its reference state. The hypothesis is that this observed 'fluidization' is a result of disrupted links between actin and myosin filaments as well as cross-linkers within the cytoskeleton and is a time-dependent effect. Here, we account for an instantaneous amplitude-dependence and apply an empirical nonlinear stress–strain relationship $E_C^* = a^* \exp(bL^*/L_0^*)$, where a^* and b are constants. We refer to this as strain-stiffening, consistent with the solid mechanics terminology (Holzapfel, 2000); this is distinct from, and not to be

TABLE 1 *Physiological dimensional parameter values. All chemical kinetic rate constants are taken from Mijailovich et al. (2000)*

Quantity	Parameter name and value
Average length of individual sarcomeres at maximum overlap	$\overline{Y}^*_{\mathrm{A}} \sim \overline{Y}^*_{\mathrm{B}} \approx 2\,\mu\mathrm{m}$ (Kuo & Seow, 2004)
Average length of an ASM cell at maximum activation	$\overline{L}^* \approx 100\,\mu\mathrm{m}$ (Stephens *et al.*, 1998)
Undeformed length of nucleus	$Z^*_0 \approx 10\,\mu\mathrm{m}$ (Kuo & Seow, 2004)
Stiffness of the cell nucleus	$E^*_{\mathrm{A}} \approx 0.7\,\mathrm{Nm}^{-1}$ (Kuo & Seow, 2004)
Extensional viscosity of the cell	$\mu^*_{\mathrm{D}} \approx 3\,\mathrm{Ns\,m}^{-1}$ (see below)
Stiffness of the cytoskeleton varies with frequency	$E^*_{\mathrm{C}} \approx 0.1 - 10\,\mathrm{Nm}^{-1}$ (Trepat *et al.*, 2007)
Number of available cross-bridges at max overlap in each sarcomere	$\overline{\rho}^*_i \approx 6 \times 10^7\,\mathrm{m}^{-1}$ (see below)
Stiffness of each cross-bridge	$K^* = 1.8 \times 10^{-3}\,\mathrm{Nm}^{-1}$ (Warshaw & Fay, 1983)
Power-stroke length	$h^* = 15.6\,\mathrm{nm}$ (Mijailovich *et al.*, 2000)
Frequency of oscillation	$\omega^* = 2\,\mathrm{Hz}$ (Bates *et al.*, 2009)
Myosin light chain kinase rate	$k^*_1 = k^*_6 = 0.06\,\mathrm{s}^{-1}$
Myosin light chain phosphorylation rate	$k^*_2 = k^*_5 = 0.1\,\mathrm{s}^{-1}$
Cycling cross-bridge attachment rate constants	$f^*_{p1} = 0.88\,\mathrm{s}^{-1}$
Cycling cross-bridge detachment rate constants	$g^*_{p1} = 0.22\,\mathrm{s}^{-1}$, $g^*_{p2} = 4(f^*_{p1} + g^*_{p1})$, $g^*_{p3} = 3g^*_{p1}$
Latch bridge detachment rate constants	$g^*_1 = 0.1\,\mathrm{s}^{-1}$, $g^*_2 = 20g^*_1$, $g^*_3 = 3g^*_1$

confused with, the post-stretch fluidization observed in the cell-level experiments (Chen *et al.*, 2010; Krishnan *et al.*, 2009). It is likely that the cell nucleus stiffens with stretch but we will assume here that E^*_{A} is constant. Finally, we assume that the cell resists deformation via an extensional viscosity μ^*_{D}.

2.2 *The Huxley–Hai–Murphy model of force generation*

The Hai–Murphy four-state model (Hai & Murphy, 1988a,b) is based on observations that myosin exists in four distinct states: (i) free unattached myosin (M^*), (ii) phosphorylated unattached myosin (M^*_{p}), (iii) phosphorylated myosin attached to actin (AM^*_{p}) (the so-called rapidly cycling cross-bridges) and (iv) de-phosphorylated myosin attached to actin (AM^*), which give rise to very slowly cycling or non-cycling cross-bridges (also called latch-bridges). The transitions from one state to another are shown in Fig. 5.

The forces generated by the sarcomeres are triggered by application of agonist and evolve with time. The Huxley–Hai–Murphy (HHM) model (Mijailovich *et al.*, 2000), based on the chemical model of Hai & Murphy (1988a) and the sliding cross-bridge model of Huxley (1957), is used to determine the magnitude of the force and shortening velocity. The equations that relate force generation by the

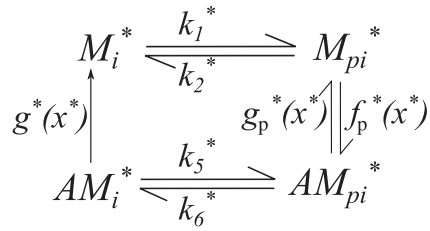

FIG. 5. Transitions between the four states accounted for in the Hai–Murphy regulation scheme.

sarcomeres to their shortening velocity are given by

$$\frac{\partial \mathbf{n}_i^*}{\partial t} - V_i^* \frac{\partial \mathbf{n}_i^*}{\partial x^*} = \mathsf{S}_i^* \mathbf{n}_i^*, \tag{2.2a}$$

$$\sum \mathbf{n}_i^* = \rho_i^*, \tag{2.2b}$$

for $i = \mathrm{A}, \mathrm{B}$, where x^* is an internal variable representing the displacement of the cross-bridges from their unstressed position, $\mathbf{n}_i^*(x^*, t^*) \equiv (M_i^*(x^*, t^*), M_{pi}^*(x^*, t^*), AM_{pi}^*(x^*, t^*), AM_i^*(x^*, t^*))$ is the number density (in x^* space) of cross-bridges in each pool, ρ_i^* is the total number of available cross-bridges per unit length of sarcomere, and the sum in (2.2b) is over the four components of $\mathbf{n}_i^*$. V_i^* is the shortening velocity of the sarcomere and is positive for contraction, so that $V_i^* = -\dot{Y}_i^*$.

In previous studies that implement the HHM model (Mijailovich *et al.*, 2000; Wang *et al.*, 2008), ρ_i^* was assumed to be constant throughout the simulation. In the model presented here, we assume that ρ_i^* for $i = \mathrm{A}, \mathrm{B}$ are either constant and maximal (i.e. $\rho_i^* = \overline{\rho}_i^*$) throughout, or piecewise constant, changing from $\overline{\rho}_i^*$ to $\overline{\rho}_i^*/2$ at a particular point in time. The reason for this choice is discussed further below.

The matrix $\mathsf{S}_i^*(x^*, t^*)$ in (2.2a) describes the probabilities of transitions between the four states, and how those probabilities depend on x^*. Phosphorylation transitions between M^* and M_p^*, and between AM^* and AM_p^* are independent of x^*. Phosphorylation of myosin facilitates interaction with actin. Transitions between M_p^* and AM_p^* and M^* and AM^* depend on x^* as the attachment of myosin heads to actin binding sites is more likely when the cross-bridge is within a powerstroke length, h^*, of the nearest binding site. Likewise, detachment is more likely outside this powerstroke length. $\mathsf{S}_i^*(x^*, t^*)$ is given in Fredberg *et al.* (1999) as

$$\mathsf{S}_i^*(x^*, t^*) = \begin{pmatrix} -k_1^* & k_2^* & 0 & g^*(x^*) \\ k_1^* & -k_2^* - f_\mathrm{p}^*(x^*) & g_\mathrm{p}^*(x^*) & 0 \\ 0 & f_\mathrm{p}^*(x^*) & -k_5^* - g_\mathrm{p}^*(x^*) & k_6^* \\ 0 & 0 & k_5^* & -k_6^* - g^*(x^*) \end{pmatrix}, \tag{2.2c}$$

where

$$(f_\mathrm{p}^*(x^*), g_\mathrm{p}^*(x^*), g^*(x^*)) = \begin{cases} (0, g_{p2}^*, g_2^*), & x^* < 0, \\ (f_{p1}^* x^*/h^*, g_{p1}^* x^*/h^*, g_1^* x^*/h^*), & 0 \leqslant x^* \leqslant h^*, \\ (0, (g_{p1}^* + g_{p3}^*)x^*/h^*, (g_1^* + g_3^*)x^*/h^*), & h^* < x^*. \end{cases} \tag{2.2d}$$

Strictly, the conservation law (2.2b) is valid only during isometric contraction (Fredberg *et al.*, 1999; Mijailovich *et al.*, 2000). Implicit in the use of this conservation law during non-isometric situations is the assumption that the distance between actin binding sites is much larger than h^*, so that there is no interference between neighbouring binding sites.

Assuming that the attached cross-bridges are linear elastic springs in parallel, and that both bound species exert equal force, the total force generated by each sarcomere is calculated by

$$F_i^* = K^* \int_{-\infty}^{\infty} x^* \mathbf{q} \cdot \mathbf{n}_i^* \, \mathrm{d}x^*, \tag{2.2e}$$

where $i = \mathrm{A}, \mathrm{B}$, K^* denotes the spring stiffness of the cross-bridges and $\mathbf{q} \equiv (0\ 0\ 1\ 1)$.

2.3 *Initial and boundary conditions*

Following the experimental protocol described in Section 1, we consider two phases. First, in the period $0 \leqslant t^* \leqslant \bar{t}^*$, we simulate isometric force generation in the presence of agonist by holding $L^* = \overline{L}^* = L_0^*$ and increasing the concentration of agonist from zero to some constant (simulated via a step change in the constants k_1^* and k_6^* from zero to the values in Table 1). We assume that initially all the cross-bridges are dephosphorylated and unbound so that

$$F_i^*(0) = 0 \quad \text{and} \quad \mathbf{n}_i^*(0) = (\rho_i^*, 0, 0, 0). \tag{2.3}$$

In the period $0 \leqslant t^* \leqslant \bar{t}^*$, we assume that the internal architecture of the cell has a particular configuration, i.e. $\overline{N}_\mathrm{A}^* = \overline{N}_\mathrm{B}^* = N_S^*/2$ (Kuo & Seow, 2004), and that there is maximal overlap between actin and myosin filaments as depicted in Fig. 4, so that $\rho_i^* = \overline{\rho}_i^*$.

In the second phase, $t > \bar{t}^*$, length-oscillations are imposed on the tissue strip. We thus prescribe a time-dependent cell length so that for the entire protocol, we write

$$L^* = \begin{cases} \overline{L}^*, & 0 \leqslant t^* \leqslant \bar{t}^*, \\ \overline{L}^* + L_\epsilon^* \sin(\omega^*(t^* - \bar{t}^*)), & t^* > \bar{t}^*, \end{cases} \tag{2.4}$$

where L_ϵ^* is the amplitude of length oscillation, and ω^* its frequency.

We wish to investigate the effect of modified or remodelled cell architecture (both internal and cytoskeletal) on force generation. We therefore assume the following possibilities for the internal architecture at $t^* = \bar{t}^*$.

(i) The internal architecture retains its initial configuration, i.e. $N_i^* = \overline{N}_i^* = 0.5 N_S^*$ and $\rho_i^* = \overline{\rho}_i^*$ for $i = \mathrm{A}, \mathrm{B}$. Current models (Politi *et al.*, 2010; Wang *et al.*, 2008) that calculate force generation in ASM via the HHM cross-bridge model assume implicitly that this is the case.

(ii) Alternatively, at $t^* = \bar{t}^*$, there is an abrupt change in internal architecture. This is conceived in response to observations of Lavoie *et al.* (2009) who propose that length fluctuations may completely disrupt actin–myosin connectivity. A mechanism that would lead to this is as follows. Imposed strain causes ρ_i^* to decrease with both increase and decrease in overlap length (as depicted in Figs 4b and c, as proposed by Herrera *et al.*, 2005) and therefore to vary continuously as a function of overlap length and hence time. At some threshold strain, ρ_i^* becomes too small for myosin to hold on to actin filaments and the contractile unit disassembles and reassembles somewhere else in the cell (i.e. a different row). The present model assumes that

the strain imposed prior to the onset of oscillations causes this disassembly and reassembly to occur instantaneously, resulting in changes in the number of row A and row B sarcomeres along with sudden reduction of ρ_i^*. We model the subsequent rearrangement as a drop in the number of sarcomeres in one row and an increase in the other row, ensuring conservation of N_S^*. Given the observation that the ratio of actin to myosin filaments is ~20:1 (Kuo *et al.*, 2003), this assumption makes sense physiologically. Thus, at $t^* = \bar{t}^*$, we assume that N_{A}^* drops to $\frac{1}{4}N_S^*$ so that $N_{\mathrm{B}}^* = \frac{3}{4}N_S^*$. The fact that there are fewer (more) contractile units in row A (B) compared with row B (A) also suggests that there will be a decrease in overlap length between actin and myosin filaments which will result in a concurrent drop in ρ_{A}^* (ρ_{B}^*) (Herrera *et al.*, 2005) as depicted in Fig. 4b and c. We arbitrarily assume here that ρ_i^* drops to $\overline{\rho}_i^*/2$. Once this architecture is established, we assume that it remains in this configuration in $t^* > \bar{t}^*$. (A more realistic mechanism would allow for these changes in ρ_i^* and N_i^* to occur dynamically and as continuous variables of overlap length which is related to our definition of sarcomere length—the distance between two dense bodies on different actin filaments (Fig. 3b and c). In this case, we would require $\rho_i^* = \rho_i^*(Y_i^*)$ and $N_i^* = N_i^*(Y_i^*)$, but this complicates the model significantly, introducing nonlinearity in the expression for the shortening velocity (see Appendix); this will further be explored in future work. We apply instantaneous changes here to ensure that this first model remains relatively simple.) The architecture description is thus given by

$$(N_{\mathrm{A}}^*, N_{\mathrm{B}}^*, \rho_{\mathrm{A}}^*, \rho_{\mathrm{B}}^*) = \begin{cases} (\overline{N}_{\mathrm{A}}^*, \overline{N}_{\mathrm{B}}^*, \overline{\rho}_{\mathrm{A}}^*, \overline{\rho}_{\mathrm{B}}^*), & 0 \leqslant t^* < \bar{t}^*, \\ (\frac{1}{4}N_S^*, \frac{3}{4}N_S^*, \frac{1}{2}\overline{\rho}_{\mathrm{A}}^*, \frac{1}{2}\overline{\rho}_{\mathrm{B}}^*), & t^* \geqslant \bar{t}^*. \end{cases} \tag{2.5}$$

The cytoskeleton is also thought to be highly malleable (Chen *et al.*, 2010; Krishnan *et al.*, 2009) with large changes in cell stiffness observed on applying transient stretch. This response, often termed 'fluidization', appears to be time-dependent one and is not accounted for here. On the other hand, the instantaneous elastic response to imposed strain is characterized by a nonlinear stress–strain relationship (referred to as 'strain-stiffening' in the solid mechanics literature). We account for such cytoskeletal changes phenomenologically via the following cases:

(A) The cytoskeletal stiffness is constant (either $E_{\mathrm{C}}^* = 0.1\ \mathrm{N\,m^{-1}}$ or $E_{\mathrm{C}}^* = 0.001\ \mathrm{N\,m^{-1}}$) .

(B) The cytoskeletal stiffness varies with strain (and hence cell length Kim *et al.*, 2011) according to

$$E_{\mathrm{C}}^* = a^*\, \mathrm{e}^{bL^*/L_0^*}, \tag{2.6}$$

where a^* and b are constants chosen to ensure that E_{C}^* varies from 0.001 to 10 $\mathrm{N\,m^{-1}}$ over a length range of ±10% of the reference length.

2.4 *Maximally activated steady state at fixed length*

In the first phase, $0 \leqslant t^* \leqslant \bar{t}^*$, the proportions of myosin in the different states evolve as the myosin phosphorylates (driven by the imposed change in k_1^* and k_6^* from 0 to $0.35\,\mathrm{s^{-1}}$) and begin to attach to the actin filament, thus generating a time-dependent force in both rows of sarcomeres. The reactions eventually settle to an activation steady state ($\overline{\mathbf{n}}_i^*$) at which the contractile force is maximal at the imposed length $\overline{L}^*$, referred to as the maximum isometric force (which we denote as $\overline{F}_i^*$) and where the

shortening velocity $\dot{Y}_i^* = 0$. In Section 2.5, we will rescale the variables with respect to this maximally activated steady-state configuration.

The length of the row B sarcomeres, in the initial isometric phase, remains constant so that

$$\overline{N_{\mathrm{B}}^*}\,\overline{Y_{\mathrm{B}}^*} = \overline{L^*}, \quad V_{\mathrm{B}}^* = 0. \tag{2.7}$$

Equation (2.2a) reduces to a system of one-dimensional equations (parametrized by x^*):

$$\frac{\partial \mathbf{n}_{\mathrm{B}}^*}{\partial t^*} = \mathsf{S}_{\mathrm{B}}(x^*)\mathbf{n}_{\mathrm{B}}^*, \tag{2.8}$$

subject to the initial condition $\mathbf{n}_{\mathrm{B}}^*(x^*, 0) = \rho_{\mathrm{B}}^*(1, 0, 0, 0)$. The time-dependent isometric solution is given by

$$\mathbf{n}_{\mathrm{B}}^*(x^*, t^*) = \sum_{k=1}^{4} a_k \mathbf{v}_k(x^*) \mathrm{e}^{\lambda_k(x^*)t^*}, \quad (0 \leqslant t^* \leqslant \bar{t}^*), \tag{2.9}$$

where a_k are constants; $\lambda_k(x^*)$ are the eigenvalues and $\mathbf{v}_k(x^*)$ the corresponding eigenvectors, of $\mathsf{S}_{\mathrm{B}}(x^*)$ satisfying $\mathsf{S}_{\mathrm{B}}\mathbf{v}_k = \lambda_k \mathbf{v}_k$. We numerically find that all but one of the eigenvalues are negative, and the remaining one is always zero (and is true for all x^*). The zero eigenvalue (equilibrium) solution satisfies the simultaneous equations

$$\mathsf{S}_{\mathrm{B}}\overline{\mathbf{n}}_{\mathrm{B}}^* = 0. \tag{2.10}$$

$\overline{\mathbf{n}}_{\mathrm{B}}^*(x^*)$ is non-zero only in the region $0 \leqslant x^* \leqslant h^*$, in which its components are

$$\overline{M_{\mathrm{p\,B}}^*}(x^*) = \frac{k_5^* k_1^*}{(1+\kappa)k_1^* k_5^* + k_1^*(k_6^* + g(x^*))\kappa + k_2^* k_5^* + g(x^*)\kappa k_5^*}, \tag{2.11a}$$

$$\overline{M^*}_{\mathrm{B}}(x^*) = \left(\frac{k_2^*}{k_1^*} + \frac{g(x^*)}{k_1^*}\kappa\right)\overline{M_{\mathrm{p\,B}}^*}(x^*), \tag{2.11b}$$

$$\overline{AM^*}_{\mathrm{B}}(x^*) = \kappa\overline{M_{\mathrm{p\,B}}^*}(x^*), \tag{2.11c}$$

$$\overline{AM_{\mathrm{p\,B}}^*}(x^*) = \frac{k_6^* + g(x^*)}{k_5^*}\kappa\overline{M_{\mathrm{p\,B}}^*}(x^*), \tag{2.11d}$$

where

$$\kappa(x^*) = \frac{f_{\mathrm{p}}(x^*)k_5^*}{(k_5^* + g_{\mathrm{p}}(x^*)) - k_5^* k_6^*}. \tag{2.11e}$$

The remaining eigenmodes decay as t^* increases but contain boundary layers of time-dependent thickness near $x^* = 0^+$ (based on numerical evidence). Since the equilibrium solution $\overline{\mathbf{n}^*}_{\mathrm{B}}(x^*)$ obtained directly from (2.10) does not include such boundary layers, the maximum isometric force calculated via (2.2e)

$$\overline{F}_{\mathrm{B}}^* = K^* \int_{-\infty}^{\infty} x^* \mathbf{q} \cdot \overline{\mathbf{n}}_{\mathrm{B}}^*(x^*)\,\mathrm{d}x^*, \tag{2.12}$$

is only the leading-order approximation.

We now consider the row A sarcomeres. These are able to shorten while the cell is held at fixed length subject to (2.1a). Thus, at maximally activated steady state, where $\dot{Y}_{\mathrm{A}}^{*}=0$,

$$\overline{N}_{\mathrm{A}}^{*}\overline{Y}_{\mathrm{A}}^{*}+\overline{Z}^{*}=\overline{L}^{*}, \tag{2.13a}$$

and from (2.1c), we obtain

$$\overline{Z}^{*}=\frac{\overline{F}_{\mathrm{A}}^{*}}{E_{\mathrm{A}}^{*}}+Z_{0}^{*}. \tag{2.13b}$$

At equilibrium, therefore, $\overline{\mathbf{n}}_{\mathrm{A}}^{*}$ will again be the zero-eigenmode, satisfying $\mathsf{S}_{\mathrm{A}}(x^{*})\overline{\mathbf{n}}_{\mathrm{A}}^{*}=0$. Again the leading order approximation for maximum isometric force $\overline{F}_{\mathrm{A}}^{*}$ is calculated via (2.2e) and can be substituted into (2.13) to obtain the equilibrium lengths $\overline{Z}^{*}$ and $\overline{Y}_{\mathrm{A}}^{*}$.

The steady-state lengths are thus given by (2.13b) and

$$\overline{Y}_{\mathrm{B}}^{*}=\overline{L}^{*}/\overline{N}_{\mathrm{B}}^{*},\quad \overline{Y}_{\mathrm{A}}^{*}=\frac{1}{\overline{N}_{\mathrm{A}}^{*}}\left(\overline{L}^{*}-Z_{0}^{*}-\frac{\overline{F}_{\mathrm{A}}^{*}}{E_{\mathrm{A}}^{*}}\right). \tag{2.14}$$

In the transients leading to equilibrium, since the row A sarcomeres are able to shorten, the shortening velocity is not zero and is given by eliminating Z^{*} from (2.1) and differentiating with respect to time so that

$$\dot{Y}_{\mathrm{A}}^{*}=-\frac{1}{\overline{N}_{\mathrm{A}}^{*}}\left(\frac{\dot{F}_{\mathrm{A}}^{*}}{E_{\mathrm{A}}^{*}}\right). \tag{2.15}$$

This is given further consideration when we consider solutions during length oscillation (see Appendix).

2.5 *Non-dimensionalization*

We non-dimensionalize lengths and stiffnesses with respect to the maximally activated steady state according to

$$\begin{gathered}L^{*}=\overline{L}^{*}L,\quad Y_{i}^{*}=\overline{Y}_{i}^{*}Y_{i},\quad Z^{*}=Z_{0}^{*}Z,\quad x^{*}=h^{*}x,\quad t^{*}=\frac{1}{\omega^{*}}t,\\ (E_{\mathrm{A}}^{*},E_{C}^{*})=E_{\mathrm{A}}^{*}(1,E_{C}),\quad T^{*}=E_{\mathrm{A}}^{*}\overline{L}^{*}T\quad\text{and}\quad F_{i}^{*}=\overline{\rho}_{i}^{*}K_{\alpha}^{*}h^{*2}F_{i},\end{gathered} \tag{2.16}$$

for $i=\mathrm{A},\mathrm{B}$, where the steady-state lengths are given by (2.14) and $\overline{L}^{*}=L_{0}^{*}$ is the unstressed cell length. Normalizing the number of sarcomeres with respect to N_{S}^{*} gives sarcomere fractions $N_{i}=N_{i}^{*}/N_{S}^{*}$ for $i=\mathrm{A},\mathrm{B}$, so that $N_{\mathrm{A}}+N_{\mathrm{B}}=1$.

Applying (2.16) together with (2.14) to (2.1a–c) yields

$$L=\frac{1}{\eta_{\mathrm{A}}}[1-\beta-\alpha_{\mathrm{A}}\overline{F}_{\mathrm{A}}]Y_{\mathrm{A}}+\beta+\alpha_{\mathrm{A}}F_{\mathrm{A}}=\frac{Y_{\mathrm{B}}}{\eta_{\mathrm{B}}}, \tag{2.17a}$$

$$\alpha_{\mathrm{A}}F_{\mathrm{A}}=\beta(Z-1), \tag{2.17b}$$

$$T=\alpha_{\mathrm{A}}F_{\mathrm{A}}+\alpha_{\mathrm{B}}F_{\mathrm{B}}+E_{\mathrm{C}}(L-1)+\tau\dot{L}, \tag{2.17c}$$

revealing the following dimensionless parameters:

$$\eta_i = \frac{\overline{N}_i}{N_i} = \frac{\overline{N}_i^*}{N_i^*}, \quad \gamma_i = \frac{\overline{Y}_i^*}{h^*}, \quad \rho_i = \frac{\rho_i^*}{\overline{\rho}_i^*}, \quad \alpha_i = \frac{\overline{\rho}_i^* K^* h^{*2}}{E_{\mathrm{A}}^* \overline{L}^*},$$
$$\beta = \frac{Z_0^*}{\overline{L}^*}, \quad E_{\mathrm{C}} = \frac{E_{\mathrm{C}}^*}{E_{\mathrm{A}}^*}, \quad \tau = \frac{\mu_{\mathrm{D}}^* \omega^*}{E_{\mathrm{A}}^*}, \tag{2.17d}$$

for $i = \mathrm{A}, \mathrm{B}$.

The dimensionless equations governing the HHM model of force generation are thus

$$\frac{\partial \mathbf{n}_i}{\partial t} + \gamma_i \dot{Y}_i \frac{\partial \mathbf{n}_i}{\partial x} = \mathsf{S}_i \mathbf{n}_i, \tag{2.18a}$$
$$\sum \mathbf{n}_i = 1, \tag{2.18b}$$

for $i = \mathrm{A}, \mathrm{B}$, $\mathbf{n}_i = (M_i, M_{pi}, AM_{pi}, AM_i)$ is the fraction of cross-bridges in each pool (i.e. $M_i = M_i^*/\rho_i^*$, etc.), and S_i is the matrix of dimensionless rate constants. The dimensionless x-dependent rate functions are given by

$$(f_{\mathrm{p}}(x), g_{\mathrm{p}}(x), g(x)) = \begin{cases} (0, g_{p2}, g_2), & x < 0, \\ (f_{p1}x, g_{p1}x, g_1 x), & 0 \leqslant x \leqslant 1, \\ (0, (g_{p1} + g_{p3})x, (g_1 + g_3)x), & x > 1, \end{cases} \tag{2.18c}$$

where $f_{p1}^* = \omega^* f_{p1}$ and so on. The dimensionless force generated by each sarcomere is then given by

$$F_i(t) = \rho_i \int_{-\infty}^{\infty} x\mathbf{q} \cdot \mathbf{n}_i(x,t)\, \mathrm{d}x, \tag{2.18d}$$

for $i = \mathrm{A}, \mathrm{B}$, where $\rho_i = \rho_i^*/\overline{\rho}_i^*$.

The dimensionless boundary and initial conditions are given by

$$\dot{Y}_i(\bar{t}) = 0, \tag{2.19a}$$
$$L(\bar{t}) = 1 + \epsilon \sin(t - \bar{t}), \tag{2.19b}$$

for $t \geqslant \bar{t}$, where $\epsilon = L_\epsilon^*/\overline{L}^*$ is the dimensionless amplitude of length oscillation. Continuity of $\mathbf{n}_i$ gives

$$\mathbf{n}_i(0^-, t) = \mathbf{n}_i(0^+, t) \quad \text{and} \quad \mathbf{n}_i(1^-, t) = \mathbf{n}_i(1^+, t). \tag{2.19c}$$

Assuming that binding sites are independent of their neighbours requires

$$AM_{pi}(x) \to 0 \quad \text{and} \quad AM_i(x) \to 0 \ \text{ as } x \to \infty \tag{2.19d}$$

with M_i and M_{pi} given by dimensionless versions of (2.10a,b) with $\kappa = 0$.

The two internal architectures are characterized by the following dimensionless parameters:

(i)

$$\eta_i = 1, \quad \rho_i = 1 \quad \text{for } t \geqslant 0 \text{ and } i = \mathrm{A}, \mathrm{B}; \tag{2.20a}$$

TABLE 2 *Dimensionless parameter values*

Parameter	Parameter value
Ratio of sarcomere numbers at non-maximally activated state to that at maximally activated state	$\eta_A = 1, 2$
Ratio of sarcomere length to powerstroke length	$\gamma_i = 100$
Ratio of available cross-bridge numbers relative to that at maximally activated state	$\rho_A = 1, 0.5$
Ratio of undeformed nucleus length to cell length	$\beta = 0.1$
Dimensionless cytoskeletal stiffness	$E_C = 0.001 - 0.1$
Dimensionless amplitude of length oscillation	$\epsilon = 0.01, 0.04$
Ratio of cross-bridge properties to cell level properties	$\alpha_i = 0.004$
Loss tangent or hysteresivity parameter	$\tau = 0.001, 0.02$
Dimensionless time at which oscillations are imposed	$\bar{t} = 20$

(ii)

$$(\eta_A, \eta_B, \rho_A, \rho_B) = \begin{cases} (1, 1, 1, 1), & 0 \leqslant t < \bar{t}, \\ (2, 0.67, 0.5, 0.5) & t \geqslant \bar{t}. \end{cases} \tag{2.20b}$$

Cytoskeletal stiffness is characterized by the following two cases:

(A)

$$E_C = 0.001 \quad \text{or} \quad 0.1; \tag{2.21a}$$

(B)

$$E_C = a e^{bL} \text{ where } a = 1.0 \times 10^{-27} \quad \text{and} \quad b = 58. \tag{2.21b}$$

The constants a and b are chosen to give the range of cytoskeletal stiffness in Table 1 when the cell length is within $\pm$ 10% of its reference length.

The time-dependent dimensionless equations (2.17) and (2.18) together with (A.1) and (A.6) are solved by recasting the equations into a form which may be solved computationally (see Appendix) using a Godunov scheme (Harten *et al.*, 1983; Roe, 1986). This scheme combines an upstream differencing finite volume method with a method-of-characteristics approach.

2.6 *Parameter values*

Dimensional parameter values are given in Table 1, and the resulting dimensionless parameters are listed in Table 2.

We determine the extensional viscosity μ_D^* in Table 1 from reported values in the literature. Deng *et al.* (2006) report values of shear storage and loss moduli (G' and G'') of ASM cells that vary with frequency. The hysteresivity, or loss tangent $\tan\delta = G''/G'$, is reported to remain fairly constant at ~0.2 over frequencies between 0.1 and 10 Hz. Typically for a Kelvin–Voigt viscoelasticity model, in which an elastic element of stiffness E^* is in parallel with a dashpot of viscosity μ^*, $\tan\delta = \mu^*\omega^*/E^*$. The reported value and the nucleus stiffness in this expression yields an extensional viscosity μ_D^* as given in Table 1, and corresponds to the larger value of the dimensionless viscosity parameter τ in Table 2.

This value for viscosity, which is based on the experiment on whole individual cells, is likely to be an effective value that combines the contributions of both cross-bridge mechanisms and cytoskeletal structure changes. In the simulations, we find that the smaller value of τ provides closer agreement of simulated force–length loops with experiment. The value used in the simulations therefore probably reflects just the cytoskeletal contribution to whole cell viscosity (see Section 4).

To estimate $\overline{\rho}_i^*$, we assume that binding sites are distributed uniformly along the actin filament with a minimum distance of h^* between them. Then under the assumption of one-to-one correspondence of cross-bridges with binding sites, we use the sarcomere length $\overline{Y}_i^*$ to determine an approximate lower bound for $\overline{\rho}_i^*$ as given in Table 1.

3. Results

Figure 6 shows the shortening velocities of the two sarcomere types V_A and V_B and corresponding contractile forces F_A and F_B plotted against time. In the isometric phase (inset of Fig. 6a), row A sarcomeres undergo shortening with a velocity V_A that increases in magnitude to a maximum, after which it decreases to zero upon reaching maximal force generation (inset of Fig. 6b). This velocity is several orders of magnitude smaller than that imposed by the subsequent length fluctuations (Fig. 6a). In the oscillatory phase, the velocities of the two sarcomere types in architecture (i) are similar, the presence of the nucleus modifying that of the row A sarcomeres slightly as indicated by the red and blue curves in Fig. 6a. The difference, however, is more exaggerated in architecture (ii) where V_A is increased significantly compared with V_B due to the decreased numbers of sarcomeres in row A. This suggests that reorganization of the internal architecture could result in changes in shortening velocity as observed experimentally (Jackson *et al.*, 2004; Jensen *et al.*, 2001; Ma *et al.*, 2002) and in model simulations (Bullimore *et al.*, 2011). In contrast to the model simulations of Bullimore *et al.* (2011) the shortening velocity changes in our model as a result of changes in strain rate; cross-bridge cycling rates $f_\mathrm{p}, g_\mathrm{p}$ and phosphorylation rate k_1 are not modified.

The contractile forces F_i corresponding to the shortening velocities in Fig. 6a are plotted against time in Fig. 6b. Force-generation during the isometric phase is identical for both row A and B sarcomeres and for both architectures (inset of Fig. 6b). At the onset of length oscillations, A and B sarcomeres in architecture (i) generate almost identical force, as would be expected by the similar shortening velocities seen in Fig. 6a. However, the amount of force that can be generated by the different sarcomere types in the two different architectures becomes evident (Fig. 6b). The significant drop in contractile force of row A and row B sarcomeres, as the architecture is modified, is particularly striking; this is a result of the reorganized contractile apparatus restricting the availability of cross-bridges. Additionally, the timescale associated with the reduction in contractile force on application of length fluctuations appears to be different for the two sarcomere types for architecture (ii); an exponential fit suggests that force generated by row A sarcomeres decays slightly quicker than row B sarcomeres (transients not shown).

Figure 7 shows the contractile force F_i, plotted against sarcomere length Y_i, where $i = \mathrm{A}, \mathrm{B}$, for the two architectures (i) and (ii) for the simulations shown in Fig. 6. For architecture (i) (Fig. 7a and b) the force–length loop for row A sarcomeres is only slightly different from that of the row B sarcomeres. B sarcomeres do not undergo length change during isometric force generation (indicated by the straight vertical black curve at $Y_\mathrm{B} = 1$) while row A sarcomeres contract from their relaxed length $Y_\mathrm{A}(0)$ (given in (A.7)) to 1. At the onset of length oscillations, the slight difference in the force–length loops between row A and row B sarcomeres is then attributed entirely to the presence of the nucleus. The force–length loops for architecture (ii) are shown in Fig. 7c and d. The straight horizontal sections of the transient curves are a result of the abrupt increase (decrease) in length of the row A (B) sarcomeres from their

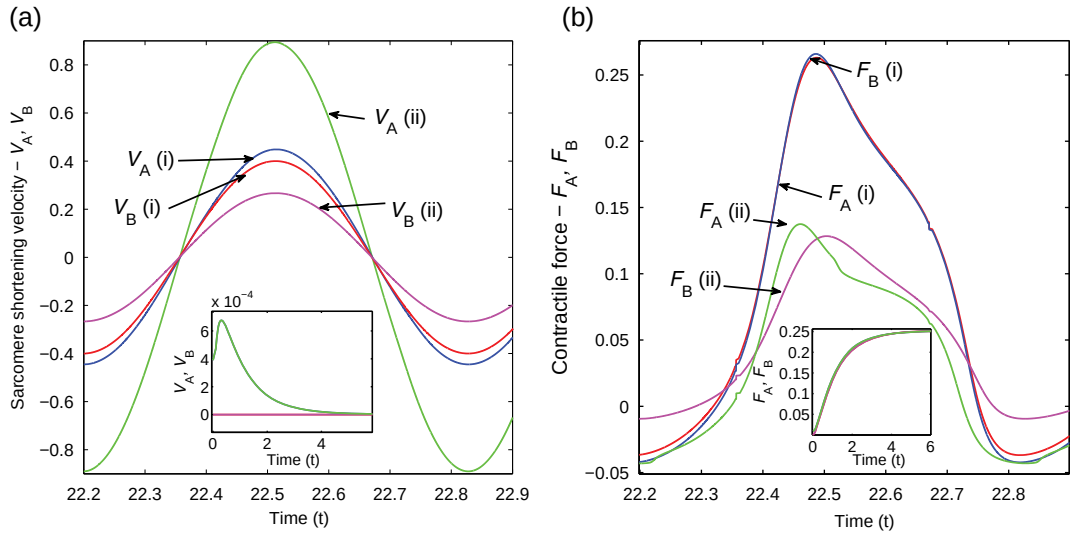

FIG. 6. Blue curves (Row A sarcomeres) and red curves (Row B sarcomere) correspond to the architecture described by (i), while the architecture described by (ii) is represented by green curves (Row A) and magenta curves (Row B); see colour version online. (a) Shortening velocity V_A and V_B plotted as a function of time during one oscillatory cycle for $\epsilon = 0.04$ many cycles after the start of the oscillatory phase in which the solution has settled to a periodic orbit. Inset: V_A and V_B as functions of time for architectures (i) and (ii) during the early part of the isometric phase $0 \leqslant t \lesssim 6$, recalling that oscillations are imposed at $\bar{t} = 20$. Only the curves for architecture (ii) are visible as they overlay the architecture (i) curves identically. (b) Contractile force F_A and F_B corresponding to shortening velocities in (a) plotted as a function of time for both oscillatory and isometric (inset) phases. Note that F_A and F_B during the oscillatory phase in architecture (i) are almost identical and thus not easily distinguishable on the graph. The same is true during the isometric phase for F_A and F_B for both architectures shown in the inset.

isometric length due to the abrupt change in N_A (N_B) imposed at $t = \bar{t}$. Thereafter, there is a significant difference between A and B sarcomeres in terms of operating length as well as the amount of force generated; the latter is a result of fewer cross-bridges (ρ_i) available relative to the maximally contracted equilibrium solution.

The cross-bridge populations $\mathbf{n}_i$ are plotted against cross-bridge position x at $t = 40$ in Fig. 8 for architectures (i) and (ii). At this time point (denoted by black asterisks in the force–length loops of Fig. 7), the sarcomere lengths are close to their minimum value and the contractile force is approximately equal to the mean. As expected, the differences in the population densities between row A and row B sarcomeres for architecture (i) is small (Fig. 8a). In contrast, the difference is significant for architecture (ii) as shown in Fig. 8b. In the latter case (architecture (ii)), the row A cycling cross-bridges (AM_{pA}) and latch bridges (AM_A) undergo more significant displacement due to the larger amplitude of oscillation. This can be seen more clearly in Fig. 9; the attached cross-bridge populations ($AM + AM_p$) for the row A sarcomeres (Fig. 9a) at various time points through the oscillatory cycle have very different shapes, are more significantly displaced and have lower peak values compared with the row B sarcomeres (Fig. 9b). Thus, within the same cell, depending on the architecture of the contractile machinery, it is possible to have a wide range of both rapidly cycling and latch-bridge populations.

Force–length loops for the whole cell for the simulations above are shown in Figs. 10–12. Simulations for architecture A(i) with baseline parameters as indicated by the caption (Fig. 10) are plotted in all three figures for reference. First, for these baseline parameter simulations (low E_C, $\tau = 0$ and relatively

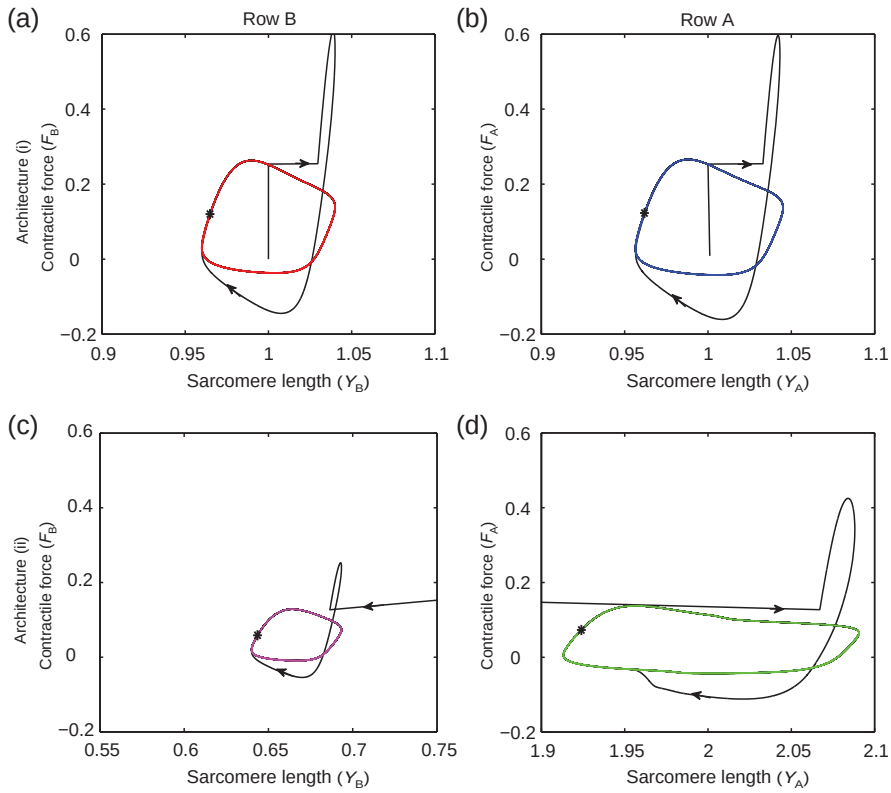

FIG. 7. Contractile force F_A plotted against sarcomere length Y_A (a,c) and F_B against Y_B (b,d), for architecture (i) (a,b) and architecture (ii) (c,d) corresponding to the simulations in Fig. 6. Colour coding (see colour version online) is identical to Fig. 6. The black curves represent the transient solutions and the black asterisks denotes the solution at $t = 40$.

stiff nucleus compared with cross-bridge stiffness (low α_i)), nonlinearity, due entirely to the cross-bridge mechanics, is immediately obvious in both architectures (Fig. 10a). The peak force in architecture A(ii) is lower than in A(i). The areas contained within the closed loops (Fig. 10b) are an indication of the magnitude of hysteresis in the system and hence the viscoelasticity that arises as a result of cycling cross-bridges. Thus, hysteresis, due entirely to cross- and latch-bridges (with $\tau = 0$) is lower for architecture A(ii) than in A(i). The loops, however, do not resemble the banana-shaped loops of Bates *et al.* (2009) (Fig. 1).

We now turn to the effect of changing internal cell architecture. One of the key parameters associated with this is α_i, increases in which may be interpreted as increased cross-bridge stiffness K^* or longer actin or myosin filament lengths, via $\overline{\rho}_i^*$, since a greater number of cross-bridges could be associated with larger overlap lengths that would stem from having longer filaments. Additionally, increased α_i could also be interpreted as increased number of rows of type i. Increasing the stiffness of either the row A or B cross-bridges (by increasing α_A or α_B) causes the cell to generate significantly higher peak force as well as increased hysteresis relative to the baseline cases in both architectures (Fig. 10a). While an increase in peak force would be expected as a result of increased cross-bridge stiffness, increased α_A or α_B could also result from longer actin and myosin filament lengths. This could explain why,

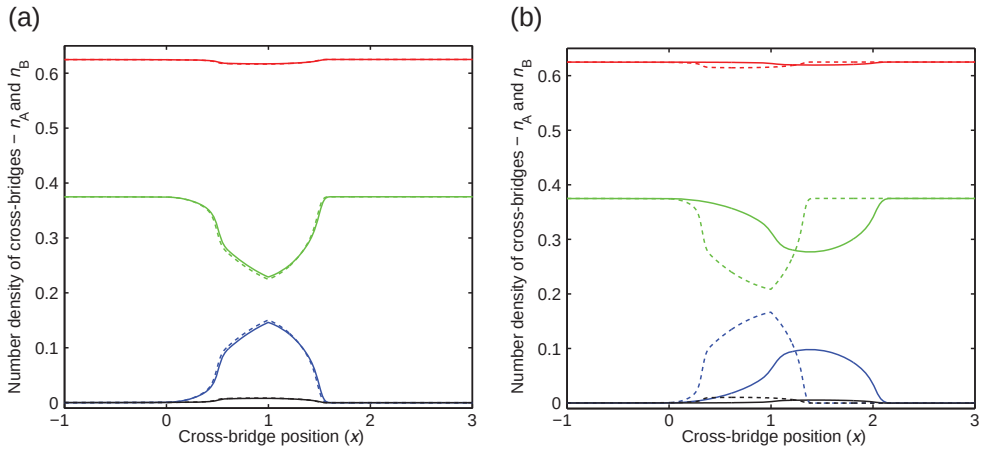

FIG. 8. Cross-bridge populations $\mathbf{n}_A$ (solid curves) and $\mathbf{n}_B$ (dashed curves) plotted against cross-bridge position x for (a) architecture (i) and (b) architecture (ii) at $t = 40$ (as marked by black asterisks in Fig. 7). Red curves represent the myosin population M_i, green, phosphorylated myosin M_{pi}, blue, rapidly cycling cross-bridges AM_{pi} and black curves represent latch bridges AM_i for $i = \mathrm{A}, \mathrm{B}$; see colour version online.

surprisingly, hysteresis is also significantly increased in both cases (Fig. 10b). Indeed it has been found that actin and myosin filaments lengths within the cell are distributed normally about a mean length and that both mean and variance can depend on degree of activation (J. Solway, personal communication). Differences between architectures (i) and (ii) are particularly striking for higher α_A or α_B (Fig. 10b); the drop in force for the rearranged architecture in case A(ii) is more significant for higher α_i, suggesting that contractile apparatus rearrangement has a much greater effect in cells with either long filaments or stiff cross-bridges.

Increasing cell viscosity τ, generates slightly greater peak forces in cases A(i) and A(ii) (Fig. 11a) and, as expected, slightly greater hysteresis (Fig. 11b). Increased cytoskeletal stiffness (with $\tau = 0$) generates significantly greater peak forces in both A(i) and A(ii) and interestingly also a significant phase shift; an additional increase in τ generates only a slight increase in peak force and hysteresis. Thus, changes in cell viscosity appear to have slightly greater impact on a more compliant cytoskeleton. The most striking feature in Fig. 11 is the significant change in shape of the force–length loops; the nonlinearity exhibited by the cross-bridge dynamics appears to be swamped by the linear cytoskeletal mechanics, although hysteresis is still evident. In all variations investigated here, peak forces and hysteresis for A(ii) were always found to be lower than those for A(i). Very small values of τ are used here to illustrate the role of the cytoskeletal viscoelasticity. Simulations for values of τ as large as those reported in Table 2 (not shown) suggest that cell hysteresis dominates the mechanical behaviour completely, with force–length loops becoming almost circular. As mentioned above, the reported value of viscosity in Table 2, which is based on experiment on whole individual cells, is likely to be an effective value that combines the contributions of both cross-bridge mechanisms and cytoskeletal structure changes. The smaller values of τ reflects just the cytoskeletal contribution. It is interesting to note that increases in α_i (Fig. 10) cause an increase in peak force but do not cause a decrease in minimum force so that the *mean* force is greater for increased cross-bridge stiffness. On the other hand, an increase in cytoskeletal stiffness increases the range of total force but the mean force varies only a little relative to the baseline cases (Fig. 11).

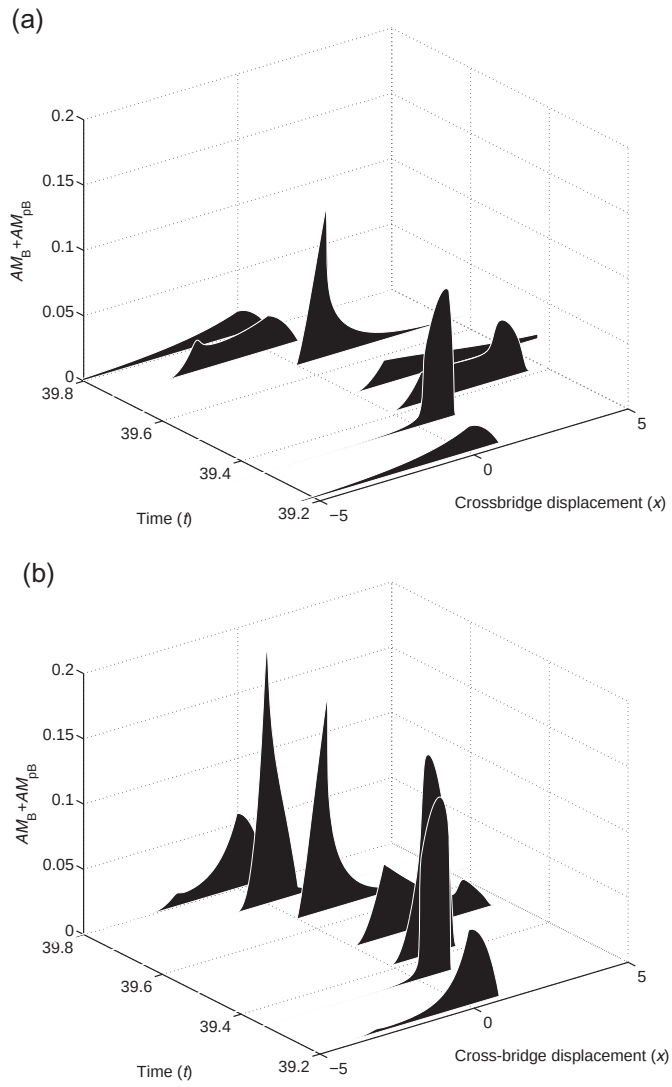

FIG. 9. Total attached cross-bridge populations $AM + AMp$ for (a) row A sarcomeres and (b) row B sarcomeres plotted against cross-bridge position x at specific time points through one oscillatory cycle for architecture (ii).

The effect of changes in cytoskeletal stiffness with cell length (Kim *et al.*, 2011) for architectures B(i) and B(ii) is shown in Fig. 12. The strain-stiffening behaviour, applied phenomenologically, so that cytoskeletal stiffness varies from $E_C = 0.001$ to $E_C = 0.1$ (to match the simulation of A(i) and A(ii) in Fig. 11) gives rise to highly nonlinear behaviour. We recall that strain-stiffening is an instantaneous elastic response characterized by a nonlinear stress–strain relationship as distinct from fluidization of cells observed immediately after transient stretch. In both architectures B(i) and B(ii), for low strains the force–time curves follow the baseline (for which $E_C = 0.001$, Fig. 12a) but then generate increased peak force upon stiffening of the cell as it increases in length (Fig. 12b). The nonlinear behaviour more

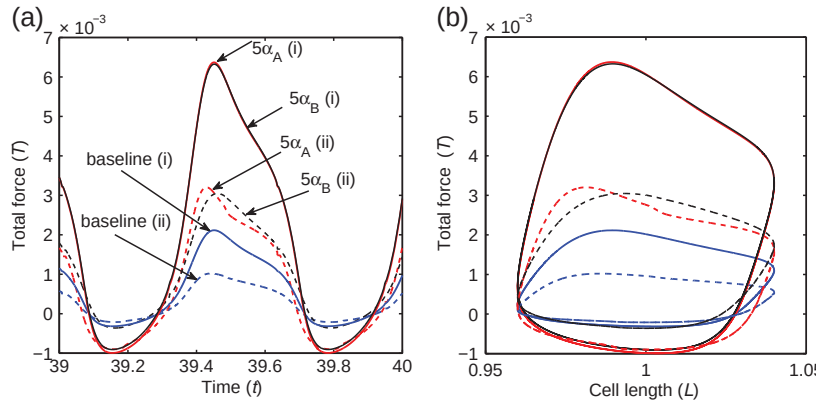

FIG. 10. (a) Total force generated by the cell, T, plotted against time for architectures A(i) (solid curves) and A(ii) (dashed curves) showing variations in cross-bridge stiffness (or filament length), α_i. Baseline parameter values are $E_C = 0.001$, $\tau = 0$, $\epsilon = 0.04$ and $\alpha_i = 0.004$ and are represented by the blue curves; see colour version online. Simulations for $\alpha_A = 0.02$ are represented by the red curves and simulations for $\alpha_B = 0.02$ are represented by black curves. (b) Total force T, plotted against cell length, L corresponding to simulations in (a). Colour coding and cases are identical to (a). Transients to this oscillatory steady state are not shown and solutions shown are for $39 \leqslant t \leqslant 40$.

closely matches the banana-shaped loops of the experimental observations in Fig.1. There are however discrepancies between the two, specifically in that the narrow end of the loops with the sharp cusp occurs at lower values of force in the experiments compared with present simulations. It is however interesting to note that only a nonlinearity in E_C (and not in τ) was required to generate the banana-shape loops. This is in contrast to the findings of Bates *et al.* (2009) in which nonlinearities in both quantities were required. This may have been partly due to the fact that their models for contractile force did not explicitly account for cross-bridge mechanisms but rather used an approximate kinetic scheme.

4. Discussion

The manner in which contractile, cytoskeletal and associated proteins interact within the cell so as to produce integrated mechanical effects (e.g. cellular contraction, stiffness or remodelling) remains a major open question (Gunst & Fredberg, 2003). In an attempt to understand these interactions, we have here developed a mechanistic model of an ASM cell that accounts for basic elements of its internal architecture, rearrangements of its contractile apparatus and changes in cytoskeletal stiffness and cell viscosity. The model is based on the conceptual models proposed by Kuo & Seow (2004), Gunst & Fredberg (2003), Herrera *et al.* (2005) and Lavoie *et al.* (2009). Contractile force generation is predicted via the HHM model (described by Mijailovich *et al.*, 2000) for a single contractile unit, with contractile units arranged both in series and in parallel within the cell. In this study, stretching was assumed to induce a single rapid rearrangement of this architecture, changing contractile unit numbers between serial and parallel configurations. The model predicts the net force generated depending on the cellular architecture, and the force–length relationships for a single cell determined by contractile and cytoskeletal components. Results from model simulations are compared against length-fluctuation tissue-strip experiments that have been extensively used (e.g. Fredberg *et al.*, 1997) and in particular the simulation results are compared with data of Bates *et al.* (2009) shown in Fig. 1.

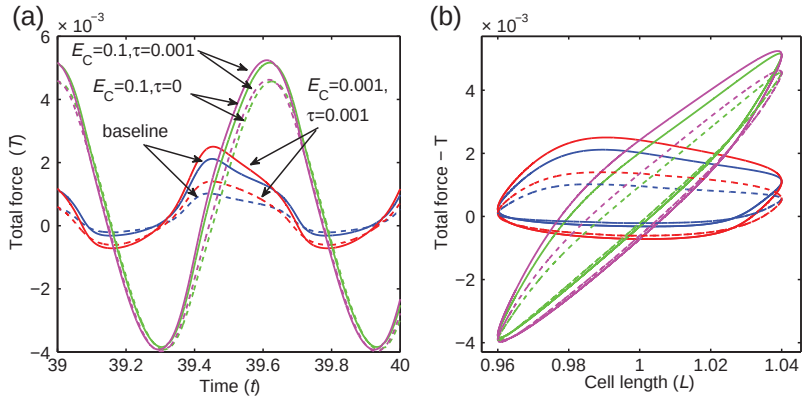

FIG. 11. (a) Total force generated by the cell, T, plotted against time for architectures A(i) (solid curves) and A(ii) (dashed curves) showing variations in cytoskeletal stiffness, E_C, and cell viscosity, τ. Baseline parameter values are $E_C = 0.001$, $\tau = 0$, $\epsilon = 0.04$ and $\alpha_i = 0.004$ and are represented by the blue curves as in Fig. 10; see colour version online. Simulations for $\tau = 0.001$ are represented by the red curves, $E_C = 0.1$ by green curves and $E_C = 0.1$, $\tau = 0.001$ by magenta curves. (b) Total force T, plotted against cell length, L corresponding to simulations in (a). Colour coding and cases are identical to (a). Transients to this oscillatory steady state are not shown and solutions shown are for $39 \leqslant t \leqslant 40$.

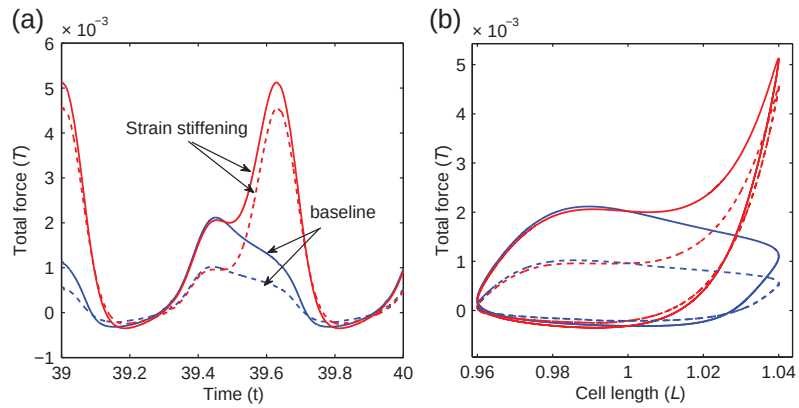

FIG. 12. (a) Total force generated by the cell, T, plotted against time for architecture (A) (blue curves) and (B) (red curves), showing the effect of introducing cytoskeletal strain-stiffening; see colour version online. Baseline parameter simulations are as for Figs 10 and 11. In all cases, solid curves represent architecture (i) and dashed curves represent architecture (ii). (b) Total force T, plotted against cell length, L corresponding to simulations in (a). Colour coding and cases are identical to (a). Transients to this oscillatory steady state are not shown and solutions shown are for $39 \leqslant t \leqslant 40$.

By taking a mechanistic approach to modelling a single ASM cell, we are able to investigate the effect of varying properties of different components within the model that have a direct physical correspondence with real cell components. The tissue-level model of Bates *et al.* (2009) takes into account elastic and visco-elastic elements and a single contractile element (which does not explicitly include cross-bridge mechanisms) in an attempt to understand the observed behaviour of activated tissue-strips undergoing length-fluctuations. Their conclusion was that both nonlinear elastic and viscoelastic components were required to generate the banana-shaped force–length loops observed in experiment. While they were able to reproduce the experimental results it is not clear what gives rise to nonlinearity or

hysteresis at the cell level in their model. Given that most experimental treatments applied to cells involve manipulation of contractile apparatus or cytoskeletal structures, (e.g. Latrunculin B, which promotes actin depolymerization, Dowell *et al.*, 2005), it is desirable to understand the contribution of these various cell-level components to observed phenomena and how different components may be targeted to obtain a particular outcome. The results from this model demonstrate a number of important cell-level interactions that could play an important role in molecular-level force generation mechanisms.

4.1 *Cell properties may be inferred from force–length loops*

The fact that cross-bridge cycling contributes to the hysteresis observed in experimental force–length loops has been known since the HHM model was developed. For example, Mijailovich *et al.* (2000) showed that cycling at higher frequencies or smaller amplitudes reduces the degree of hysteresis. Our model incorporates two main sources of hysteresis: cross-bridge cycling and cell viscosity. However, they affect hysteresis very differently. Increased hysteresis with increased peak tensile force without increased peak compressive force suggests either relatively high cross-bridge stiffness or large filament (or overlap) length (Fig. 10). If the cell also strain-stiffens, the width of the force–length loop is maintained at low strains, generating a sharp cusp at peak tensile force (Fig. 12). Increased cell viscosity has a different effect; at low cytoskeletal stiffnesses there is an overall increase in the width of the loop (Fig. 11), with increases in peak tensile and compressive forces. The increased width is also maintained at low strain when the cell strain-stiffens, so that the cusp at peak tensile force is maintained (Fig. 12). The other difference between these two hysteresis-generating mechanisms is that nonlinearity, clearly evident from the cross-bridge cycling, is further exaggerated for large cross-bridge stiffness or filament length, but gets swamped by large cell viscosity, with force–length loops becoming circular. The components we have included in the model so far are not able to reproduce the cusp at the low-strain end of the force–length loop (Fig. 1). Model simulations also suggest that cytoskeletal viscosity (τ) may be estimated from a knowledge of whole cell extensional viscosity and prediction of hysteresivity from the cross-bridge mechanisms. A further potential source of hysteresis may be length adaptation that results from sarcomere or cytoskeletal reorganization, which has not been accounted for here.

Cytoskeletal stiffness is also evident from the force–length loops of the whole cell. Increases in both peak tensile and peak compressive forces indicate increases in cytoskeletal stiffness, without strain-stiffening (Fig. 11). The nonlinearity due to cross-bridge cycling can be swamped by the large linear cytoskeletal stiffness, although hysteresis is maintained (Fig. 12). Phase-shifts in the force–time plot are also related to increases in cytoskeletal stiffness (Fig. 11). Neither the changes in cross-bridge stiffness nor changes in strain-independent stiffness are capable of generating the force–length loops resembling the experimentally observed banana-shape (Fig. 12). One way in which the current model is able to generate force–length loops that more closely resembles the banana-shaped loops is through the incorporation of a nonlinear stress–strain relationship to characterize instantaneous changes in cytoskeletal stiffness. Furthermore, the strain-stiffening behaviour also accounts for the change in force–length loop shapes as the amplitude of length fluctuations is varied, as observed by Fredberg *et al.* (1997) (results not shown). There are numerous additional possible sources of nonlinearity that we have not included here. Inferences about strain-stiffening may have to be modified upon further exploration of these additional elements.

4.2 *Transitions from serial to parallel configurations play a quantifiable role in force generation*

The change in architecture in this model is conceived in response to observations of Lavoie *et al.* (2009), who proposed that length fluctuations may disrupt actin–myosin connectivity. The present

model accounts for such internal rearrangement brought about instantaneously at the onset of oscillation. Despite the total number of contractile units being conserved between both architectures (i) and (ii), the cell's contractile force is modified significantly by contractile apparatus rearrangement when the cytoskeleton is relatively compliant, the cross-bridges are stiffer than the nucleus, and filament lengths are relatively long. Additionally the length about which the sarcomeres oscillate is perturbed significantly from its equilibrium value (Figs 7c and d). A drop in the number of row A sarcomeres, and hence also the number of available cross-bridges, results in a smaller force being generated by these sarcomeres. The associated increase in row B sarcomeres and consequent reduction in number of available cross-bridges also results in a decrease in contractile force. Thus, the overall effect is a drop in the total contractile force. Creation of additional rows would further affect the total contractile force with a relative pay-off between increased parallel sarcomeres versus decreased available cross-bridges. Although we have assumed only two rows, our model can represent the possibility of increased rows provided the parameters α_i and ρ_i are chosen appropriately.

We note that constant ρ_i is effectively the small-deformation limit of situations in which ρ_i may vary with overlap length. Large deformations cause large changes in overlap length between actin and myosin filaments, thus reducing the total number of cross-bridges available for binding. Additionally, the oscillation amplitudes applied here generate a significant difference in rapidly cycling and latch bridge populations in row A compared with those of row B (Fig. 8b). The simple conservation law (2.2) assumes that the distance between binding sites is much greater than h^*. The larger the amplitude of oscillation (particularly in row A sarcomeres), the more unrealistic this assumption becomes, since latch-bridges take large excursions out of the power-stroke region. We have assumed here that the transition from row A to row B occurs instantaneously. An extension to this model could allow for these transitions to occur over some finite time. Further refinement of the model will thus demonstrate the effect of dynamic changes by incorporating a more realistic mechanism that allows for contractile units to disassemble and reassemble.

4.3 *Contractile apparatus rearrangement causes significant change in shortening velocity*

A relationship between increased ASM shortening velocity and airway hyper-responsiveness has been suggested both experimentally (Bullimore *et al.*, 2011; Jackson *et al.*, 2004; Jensen *et al.*, 2001; Ma *et al.*, 2002) and via the use of model simulations (Bullimore *et al.*, 2011). Other experimental observations suggest a relationship between shortening velocity and myosin filament density (Smolensky *et al.*, 2005). We have shown that the shortening velocity of sarcomeres that attach to the cytoskeleton via the nucleus is modified both by the mechanical properties of the cell nucleus and by changes in the architecture of the cell (Fig. 6a). The modifications are a result of changes in strain rate; cross-bridge cycling rates f_p, g_p and phosphorylation rate k_1 are not modified here. In contrast, it is these rates that are modified to generate changes in shortening velocity in the model simulations of Bullimore *et al.* (2011) to investigate the relationship between increased shortening velocity and hyper-responsiveness. Interestingly, and in contrast to their findings, the architecture change chosen for these simulations, which caused an increased shortening velocity of row A sarcomeres (Fig. 6a), was accompanied by a *reduction* in corresponding contractile force (Fig. 6b). Nucleus deformation in an activated ASM cell is evident from electron microscopy of its ultrastructure (Kuo & Seow, 2004) and so is likely to have an effect on the shortening velocity of type A sarcomeres in the manner we have outlined. If the nucleus is sufficiently stiff, however, or stiffens instantaneously with imposed stretch, then the shortening velocity of row A sarcomeres will approximate the cell shortening velocity. Here, we have assumed a relatively compliant nucleus and for this, along with an increase in row A shortening velocity, the

shortening velocity of row B sarcomeres drops relative to that of architecture (i). In this model, we are able to apply length changes and predict the force generated. The inverse problem of applying force oscillations, and predicting length changes is a non-trivial initial value problem, for which a numerical solution has been proposed (Bullimore *et al.*, 2011) and could be used in future work. At this time, however, we are not able to investigate how force-oscillation-driven internal remodelling affects shortening velocity. We have shown however, that architecture changes affect shortening velocity of some of the sarcomeres and suggest that architecture changes may thus contribute to the factors that cause airway hyper-responsiveness.

In summary, we have combined a number of conceptual models into a mathematical model of an individual ASM cell. We have shown how remodelling of the internal and external structures of the cell significantly modifies the mechanical behaviour of the cell. Given the very different effects of the contractile apparatus and cytoskeletal behaviour and their interaction, we propose ways in which cell properties may be inferred from force–length loops. We show that contractile force, shortening velocity and sarcomere operating lengths vary as the internal cell architecture is altered, and that force generation and hysteresis characteristics depend strongly on interactions between internal and external structures. We believe this bottom-up approach that accounts for cell structure is crucial in understanding how molecular mechanisms within the ASM cell affect airway properties in the diseased lung.

Funding

B.S.B. is supported by a New Investigator Research Grant funded by the Medical Research Council (G0901174).

References

Bates, J. H. T., Bullimore, S. R., Politi, A. Z., Sneyd, J., Anafi, R. C. & Lauzon, A. M. (2009) Transient oscillatory force–length behavior of activated airway smooth muscle. *AJP: Lung Cellular and Molecular Physiology*, **297**, L362–L372.

Brightling, C. E., Gupta, S., Gonem, S. & Siddiqui, S. (2012) Lung damage and airway remodelling in severe asthma. *Clinical and Experimental Allergy*, 42, 638–649.

Brook, B. S., Peel, S. E., Hall, I. P., Politi, A. Z., Sneyd, J., Bai, Y., Sanderson, M. J. & Jensen, O. E. (2010) A biomechanical model of agonist-initiated contraction in the asthmatic airway. *Respiratory Physiology & Neurobiology*, **170**, 44–58.

Bullimore, S. R., Siddiqui, S., Donovan, G. M., Martin, J. G., Sneyd, J., Bates, J. H. T. & Lauzon, A.-M. (2011) Could an increase in airway smooth muscle shortening velocity cause airway hyperresponsiveness? *AJP: Lung Cellular and Molecular Physiology*, **300**, L121–L131.

Chen, C., Krishnan, R., Zhou, E., Ramachandran, A., Tambe, D., Rajendran, K., Adam, R. M., Deng, L. & Fredberg, J. J. (2010) Fluidization and resolidification of the human bladder smooth muscle cell in response to transient stretch. *PLoS ONE*, **5**, e12035.

Deng, L., Trepat, X., Butler, J. P., Millet, E., Morgan, K. G., Weitz, D. A. & Fredberg, J. J. (2006) Fast and slow dynamics of the cytoskeleton. *Nature Materials*, **5**, 636–640.

Dowell, M. L., Lakser, O. J., Gerthoffer, W. T., Fredberg, J. J., Stelmack, G. L., Halayko, A. J., Solway, J. & Mitchell, R. W. (2005) Latrunculin b increases force fluctuation-induced relengthening of ach-contracted, isotonically shortened canine tracheal smooth muscle. *Journal of Applied Physiology*, **98**, 489–497.

Dowell, M. L., Lavoie, T. L., Lakser, O. J., Dulin, T. L. N., Fredberg, J. J., Gerthoffer, W. T., Seow, C. Y., Mitchell, R. W. & Solway, J. (2010) Mek modulates force-fluctuation-induced relengthening of canine tracheal smooth muscle. *European Respiratory Journal*.

Fredberg, J. J., Inouye, D. S., Mijailovich, S. M. & Butler, J. P. (1999) Perturbed equilibrium of myosin binding in airway smooth muscle and its implications in bronchospasm. *American Journal of Respiratory and Critical Care Medicine*, **159**, 959–967.

Fredberg, J. J., Inouye, D. S., Miller, B., Nathan, M., Jafari, S., Raboudi, S. H., Butler, J. P. & Shore, S. A. (1997) Airway smooth muscle, tidal stretches, dynamically determined contractile states. *American Journal of Respiratory and Critical Care Medicine*, **156**, 1752–1759.

Gunst, S. J. & Fredberg, J. J. (2003) The first three minutes: smooth muscle contraction, cytoskeletal events, and soft glasses. *Journal of Applied Physiology*, **95**, 413–425.

Gunst, S. J., Meiss, R. A., Wu, M. F. & Rowe, M. (1995) Mechanisms for the mechanical plasticity of tracheal smooth muscle. *American Journal of Physiology - Cell Physiology*, **268**, C1267–C1276.

Gunst, S. J. & Zhang, W. (2008) Actin cytoskeletal dynamics in smooth muscle: a new paradigm for the regulation of smooth muscle contraction. *American Journal of Physiology-Cell Physiology*, **295**, C576–C587.

Hai, C.-M. & Murphy, R. A. 1988a Cross-bridge phosphorylation and regulation of latch state in smooth muscle. *American Journal of Physiology*, **254** (*Cell Physiol*. 23): C99–C106.

Hai, C.-M. & Murphy, R. A. 1988b Regulation of shortening velocity by cross-bridge phosphorylation in smooth muscle. *American Journal of Physiology*, **255** (*Cell Physiol*. 24): C86–C94.

Harten, A., Lax, P. D. & Vanleer, B. (1983) On upstream differencing and Godunov-type schemes for hyperbolic conservation-laws. *SIAM Review*, **25**, 35–61.

Herrera, A. M., McParland, B. E., Bienkowska, A., Tait, R., Paré, P. D. & Seow, C. Y. (2005) 'sarcomeres' of smooth muscle: functional characteristics and ultrastructural evidence. *Journal of Cell Science*, **118**(Pt 11), 2381–92.

Holzapfel, G. (2000) *Nonlinear Solid Mechanics : a Continuum Approach for Engineering.* Chichester: Wiley.

Huxley, A. (1957) Muscle structure and theories of contraction. *Program in Biophysics and Biophysical Chemistry* **7**, 255–318.

Jackson, A. C., Murphy, M. M., Rassulo, J., Celli, B. R. & Ingram, R. H. (2004) Deep breath reversal and exponential return of methacholine-induced obstruction in asthmatic and nonasthmatic subjects. *Journal of Applied Physiology*, **96**, 137–142.

Jensen, A., Atileh, H., Suki, B., Ingenito, E. P. & Lutchen, K. R. (2001) Airway caliber in healthy and asthmatic subjects: effects of bronchial challenge and deep inspirations. *Journal of Applied Physiology*, **91**, 506–515.

Kim, T., Hwang, W. & Kamm, R. D. (2011) Dynamic role of cross-linking proteins in actin rheology. *Biophysical Journal*. URL http://www.sciencedirect.com/science/article/pii/S000634951101006X.

Krishnan, R., Park, C. Y., Lin, Y.-C., Mead, J., Jaspers, R. T., Trepat, X., Lenormand, G., Tambe, D., Smolensky, A. V., Knoll, A. H., Butler, J. P. & Fredberg, J. J. (2009) Reinforcement versus fluidization in cytoskeletal mechanoresponsiveness. *PLoS ONE*, **4**, e5486.

Kuo, K.-H., Herrera, A. M. & Seow, C. Y. (2003) Ultrastructure of airway smooth muscle. *Respiratory Physiology & Neurobiology*, **137**, 197–208.

Kuo, K.-H. & Seow, C. Y. (2004) Contractile filament architecture and force transmission in swine airway smooth muscle. *Journal of Cell Science*, **117**, 1503–1511.

Lambert, R. K. (2004) Mathematical description of geometric and kinematic aspects of smooth muscle plasticity and some related morphometrics. *Journal of Applied Physiology*, **96**, 469–476.

Lauzon, A.-M., Bates, J. H. T., Donovan, G. M., Tawhai, M. H., Sneyd, J. & Sanderson, M. J. A multiscale approach to airway hyperresponsiveness: from molecule to organ. *Frontiers in Physiology*, 3: 1–25, 2012.

Lavoie, T. L., Dowell, M. L., Lakser, O. J., Gerthoffer, W. T., Fredberg, J. J., Seow, C. Y., Mitchell, R. W., & Solway, J. (2009) Disrupting actin-myosin-actin connectivity in airway smooth muscle as a treatment for asthma? *Proceedings of the American Thoracic Society*, **6**, 295–300.

Ma, X., Cheng, Z., Kong, H., Wang, Y., Unruh, H., Stephens, N. L. & Laviolette, M. (2002) Changes in biophysical and biochemical properties of single bronchial smooth muscle cells from asthmatic subjects. *American Journal of Physiology - Lung Cellular Molecular Physiology*, **283**, L1181–L1189.

Mehta, D. & Gunst, S. J. (1999) Actin polymerization stimulated by contractile activation regulates force development in canine tracheal smooth muscle. *The Journal of Physiology*, **519**, 829–840.

Mijailovich, S. M., Butler, J. P. & Fredberg, J. J. (2000) Perturbed equilibria of myosin binding in airway smooth muscle: Bond-length distributions, mechanics, and atp metabolism. *Biophysical Journal*, **79**, 2667–2681.

Politi, A. Z., Donovan, G. M., Tawhai, M. H., Sanderson, M. J., Lauzon, A.-M., Bates, J. H. T. & Sneyd, J. (2010) A multiscale, spatially distributed model of asthmatic airway hyper-responsiveness. *Journal of Theoretical Biology*, **266**, 614–624.

Pratusevich, V. R., Seow, C. Y. & Ford, L. E. (1995) Plasticity in canine airway smooth muscle. *The Journal of General Physiology*, **105**, 73–94.

Roe, P. L. (1986) Characteristic-based schemes for the Euler equations. *Annual Review of Fluid Mechanics*, **18**, 337–365.

Silveira, P. S. P., Butler, J. P. & Fredberg, J. J. (2005) Length adaptation of airway smooth muscle: a stochastic model of cytoskeletal dynamics. *Journal of Applied Physiology*, **99**, 2087–2098.

Smolensky, A. V., Ragozzino, J., Gilbert, S. H., Seow, C. Y. & Ford, L. E. (2005) Length-dependent filament formation assessed from birefringence increases during activation of porcine tracheal muscle. *Journal of Physiology*, **563**, 517–527.

Stephens, N. L., Li, W., Wang, Y. & Ma, X. (1998) The contractile apparatus of airway smooth muscle. biophysics and biochemistry. *American Journal of Respiratory and Critical Care Medicine*, **158**, S80–S94.

Trepat, X., Deng, L., An, S. S., Navajas, D., Tschumperlin, D. J., Gerthoffer, W. T., Butler, J. P. & Fredberg, J. J. (2007) Universal physical responses to stretch in the living cell. *Nature*, **447**, 592–595.

Wang, I., Politi, A. Z. , Tania, N., Bai, Y., Sanderson, M. J. & Sneyd, J. (2008) A mathematical model of airway and pulmonary arteriole smooth muscle. *Biophysical Journal*, **94**, 2053–2064.

Warshaw, D. & Fay, F. S. (1983) Cross-bridge elasticity in single smooth muscle cells. *Journal of General Physiology*, **82**, 157–199.

Zhang, W. & Gunst, S. J. (2008) Interactions of airway smooth muscle cells with their tissue matrix: implications for contraction. *Proceedings of the American Thoracic Society*, **5**, 32–39.

Appendix A

A.1 *Solution of governing equations*

At any time, t, (2.17b) gives Y_{B} as function of time so that the velocity imposed on the row B sarcomeres is given by

$$\dot{Y}_{\mathrm{B}} = \begin{cases} 0, & 0 \leqslant t \leqslant \bar{t}, \\ \epsilon \eta_{\mathrm{B}} \cos(t - \bar{t}), & t > \bar{t}. \end{cases} \tag{A.1}$$

Substituting this into (2.18) for $i = \mathrm{B}$ allows determination of $\mathbf{n}_{\mathrm{B}}(x, t)$ and hence $F_{\mathrm{B}}(t)$. Rearranging (2.17a) for Y_{A} and differentiating with respect to time gives

$$\dot{Y}_{\mathrm{A}} = \eta_{\mathrm{A}} \frac{\dot{L} - \alpha_{\mathrm{A}} \dot{F}_{\mathrm{A}}}{1 - \beta - \alpha_{\mathrm{A}} \overline{F}_{\mathrm{A}}}, \tag{A.2}$$

assuming N_{A} is constant. Differentiating (2.18d) with respect to time gives

$$\dot{F}_{\mathrm{A}} = \rho_{\mathrm{A}} \int_{-\infty}^{\infty} x\mathbf{q} \cdot \left(-\gamma_{\mathrm{A}} \dot{Y}_{\mathrm{A}} \frac{\partial \mathbf{n}_{\mathrm{A}}}{\partial x} + \mathsf{S}_{\mathrm{A}} \mathbf{n}_{\mathrm{A}} \right) \mathrm{d}x, \tag{A.3}$$

using (2.18a) and assuming that ρ_A remains constant. The first term in the integral can be integrated by parts giving

$$\dot{F} = \rho_A(\gamma_A \dot{Y}_A \mathcal{H}_2(t) + \mathcal{H}_1(t)), \tag{A.4}$$

where

$$\mathcal{H}_1(t) = \int_{-\infty}^{\infty} x\mathbf{q} \cdot \mathsf{S}_A \mathbf{n}_A \, dx, \tag{A.5a}$$

$$\mathcal{H}_2(t) = \int_{-\infty}^{\infty} \mathbf{q} \cdot \mathbf{n}_A \, dx. \tag{A.5b}$$

Substituting for $\dot{F}_A$ into the expression for $\dot{Y}_A$ (A.2), and solving for $\dot{Y}_A$ yields

$$\dot{Y}_A = \frac{\dot{L}(t) - \alpha_A \rho_A \mathcal{H}_1(t)}{(1/\eta_A)(1 - \beta - \alpha_A \overline{F}_A) + \alpha_A \rho_A \gamma_A \mathcal{H}_2(t)}, \tag{A.6}$$

where $\dot{L}(t) = \dot{Y}_B(t)/\eta_B$. This expression for $\dot{Y}_A$ then used in (2.18) for $i = A$ to determine $\mathbf{n}_A(x,t)$ and $F_A(t)$. At any time t, having calculated $F_A(t)$, the sarcomere lengths for the A contractile units is given by

$$Y_A(t) = \eta_A \frac{L - \beta - \alpha_A F_A}{1 - \beta - \alpha_A \overline{F}_A}. \tag{A.7}$$

Comparing this with the equation for Y_B (2.17b), we note how the elasticity of the cell nucleus modifies the behaviour of the row A sarcomeres. It is then possible to determine the time-dependent tension on the cell via (2.17d) and (2.17c) yields $Z(t)$.

The time-dependent dimensionless equations (2.18) together with (A.1) and (A.6) are solved computationally subject to the initial and boundary conditions (2.19), using a Godunov scheme (Harten *et al.*, 1983; Roe, 1986). This scheme combines an upstream differencing finite volume method with a method-of-characteristics approach. To ensure simulation results were accurate, the code was validated by comparing results obtained with the Godunov scheme on a single sarcomere, and corresponding results obtained using a predictor-corrector McCormack scheme; solutions were identical. The numerical artefacts in Fig. 6 appear in every cycle and are a result of having to apply a CFL stability condition for values of shortening velocity larger than some threshold value in the solution of the Godunov scheme. If applied to very small values of shortening velocity the corresponding time steps get very large, which, although allow stability for the PDE solution, causes problems with the chemical kinetics steps of the solution procedure.